Acoustic Radiation from Instability Waves within Supersonic Jets Obtained via Theory and Large-Eddy Simulation

Jianhui Cheng,* Weiqi Shen,† and Steven A. E. Miller‡
University of Florida, Gainesville, Florida, 32611, USA

The impact of large-scale turbulent structures on the aerodynamic flow-field and far-field radiated noise is investigated through analysis of an under-expanded heated supersonic jet. The onset and statistics of these structures are examined via well-established instability wave theory and large-eddy simulation (LES). The jet operating conditions are M_j = 1.469, total temperature ratio 3.20, and Reynolds number 6.26×10^5. Predicted instability wave shape functions show good agreement with wavenumber space of LES in near-nozzle regions for azimuthal modes zero and one. A stochastic theory and the Ffowcs Williams-Hawkings equation are used to predict radiated noise from the instability waves and LES, respectively. Sound pressure levels at the peak jet noise frequency in the far-field are in relative agreement between instability theory, LES, and experimental measurement. The noise in the upstream radiation direction is dominated by the fine-scale and broadband shock-associated noise, which is well predicted by LES that agrees with measurement. Acoustic radiation in the upstream direction from the instability waves is dominated by other noise sources but present and quantified. Limitations of linear instability theory are apparent for jet flow-fields that contain shock-cell structures.

Nomenclature

Symbols	Description
A, B	Amplitude or amplitude function
D	Nozzle exit diameter
$\hat{g}$	Wavenumber spectrum
$\mathcal{H}$	Heaviside function
i	Imaginary part
m	Azimuthal mode number
p	Pressure
$\hat{p}$	Shape function of pressure
$\boldsymbol{q}$	Flow-field variables
R	Distance
R_j	Radius of the nozzle
$\tilde{S}$	Power spectrum
T	Temperature
T_{ij}	Lighthill's stress tensor
t	Time
u_j	Jet fully-expanded exit velocity
u_p	Phase speed
$\overline{\boldsymbol{V}}$	Velocity vector
$\boldsymbol{V'}$	Velocity perturbation vector
Subscripts	
n	Order of flow properties
$\hat{n}$	Normal direction
∞	Ambient or infinity
Greek Symbols	
α	Wavenumber
β	Non-parallel correction factor
γ	Ratio of specific heats
δ	Dirac delta function
δ_n	Gauge function of asymptotic expansion
δ_{ij}	Kronecker delta function
ϵ	Small parameter
η	Scaled wavenumber
τ	Retarded time
Φ	Phase lag
ψ	Polar angle
ω	Radial frequency
ρ	Density
ρ_j	Fully expanded density
Non-Dimensional Numbers	
M_j	Fully expanded Mach number
St	Strouhal number
Re	Reynolds number

I. Introduction

Jet noise from fighter aircraft remains one of the major sources of noise during aircraft carrier operations, near military airfields, and consistently contributes to significant hearing loss even with the most advanced hearing protection.

*Ph.D. Candidate, Department of Mechanical and Aerospace Engineering, University of Florida, 231 MAE-A, P.O.Box 116250, chengjianhui@ufl.edu, AIAA Student member.

†Ph.D. Candidate, Department of Mechanical and Aerospace Engineering, University of Florida, 231 MAE-A, P. O. Box 116250, weiqishen1994@ufl.edu, AIAA Student member.

‡Assistant Professor, Department of Mechanical and Aerospace Engineering, University of Florida, 231 MAE-A, P. O. Box 116250, saem@ufl.edu, AIAA Senior / Lifetime member.

Therefore, determining the noise source, propagation, and methods to control noise via analytical and experimental approaches are necessary. It is generally accepted that there are three basic components of supersonic jet noise. These are turbulent mixing noise, broadband shock-associated noise (BBSAN), and the screech tones [1]. The latter two jet noise sources appear predominantly in off-design jets. Tam et al. [2] argued that turbulent mixing noise is associated with fine-scale turbulence and large-scale turbulent structures.

The acoustic analogy is a method to predict noise based on the equations of motion and to relate radiated noise to equivalent analogous sources. Lighthill [3] rearranged the Navier-Stokes equations into a wave operator and equivalent source. He solved this equation with the method of the Green's function. Ffowcs Williams [4] investigated the effects of convection of turbulent structures within jets and showed that the radiation dependence is proportional to u_j^3 at supersonic convection speeds, where u_j is the fully-expanded jet velocity. Lilley [5] and Goldstein [6] accounted for the refraction effects via separating the flow-field into a mean and perturbation flow-field quantity, and illustrated the effect of the presence of solid bodies. Recently, Miller [7] proposed a comprehensive model using an acoustic analogy that has been used to compute the BBSAN.

The instability wave theory used to compute the noise radiated from the large-scale turbulent structures in a plane turbulent shear layer was developed by Morris and Tam [8]. Tam and Burton [9, 10] extended this method by separating the flow-field into the inner and outer region, and applied the matched asymptotic expansion. The far-field pressure was predicted and validated by an axisymmetric jet at $M_j = 2$. Dahl [11] adopted this method for supersonic coaxial jets, and the computed results (directivity pattern) agreed well with the measurements. Tam and Hu [12] showed that the Kelvin-Helmholtz instability waves are responsible for the formation of large-scale turbulent structures. The phase speed of instability waves is responsible for the efficiency and directionality of the radiated noise. Tam and Chen [13] quantified the effects of the whole instability wave by applying a stochastic turbulence theory [14]. Mohseni [15] verified the assumption of instability wave theory of Tam by comparing direct numerical simulation (DNS), linear Navier-Stokes (LNS) simulation, and instability wave solutions. The amplitude of the instability wave was scaled with the simulation results, and the comparisons were used to illustrate the sound generation mechanism for Mach wave radiation. Recently, the bi-orthogonal and proper orthogonal decomposition (POD) methods were used to extract the instability waves from DNS, LES, or experiments to explain the contributions of the instability waves. These methods were used to determine the amplitude of the instability wave from linear stability theory or parabolized stability equations (PSE) for subsonic, transonic, and supersonic jets [16–18].

The objective of our research is to explore the connection between the shear flow turbulence and the radiated noise, particularly on the relationship between large-scale turbulent structures and noise of hot supersonic jets. In the present study, we compute the jet noise of an imperfectly expanded and heated supersonic jet from large-scale turbulent structures in the upstream and downstream directions via the instability wave theory of Tam [9, 10, 13]. Large-eddy simulation (LES) provides the turbulent statistics in the jet shear layer. The Ffowcs Williams-Hawkings (FWH) approach is used to compute the radiated far-field noise based on the LES. We use the mean velocity and density from the LES to find the solution of the instability waves, including the local wavenumbers and shape functions at several azimuthal modes. The shape functions and perturbations at various axial positions are compared with the LES results. The comparison of radiated noise between the prediction, LES, and measurements is presented. The measurements are from a hot under-expanded supersonic jet from the NASA Small Hot Jet Acoustic Rig (SHJAR) database [19]. These methods facilitate our understanding of the noise generation process from large-scale turbulent structures for the eventual use in a new control algorithm under development.

II. Methodology

A. Large–Eddy Simulation Database

An open-source LES code called High-Fidelity Large-Eddy Simulation (HiFiLES) [20] is modified to simulate supersonic jet flows. HiFiLES is a high-order compressible Navier-Stokes solver based on the energy-stable flux reconstruction (ESFR) scheme [21]. Compared to other high-order methods, this method unifies many existing approaches such as the discontinuous Galerkin (DG) scheme [22] and the spectral difference method [23] with a simplified implementation. The high-order accuracy ESFR schemes are achieved by using high-order polynomials to approximate the solution inside each element. A correction function is chosen to account for the common interface flux and to reconstruct the continuous flux function inside the element. On the interfaces of the elements, the Harten-Lax-van Leer-Contact (HLLC) [24] Riemann solver is used to compute the common numerical flux. Details of the numerical methods can be found within Huynh [25, 26], Vincent et al. [21], and Castonguay et al. [27].

We use our LES solver to simulate an under-expanded hot supersonic jet from the SHJAR database [19]. The nozzle is the circular convergent small metal chevron number 000 (SMC000) designed by NASA Glenn Research Center. The nozzle exit diameter is 0.0508 m with lip thickness of approximately 2.5% of the nozzle diameter. At the nozzle inlet, a characteristic based subsonic inlet boundary condition is specified using total pressure and total temperature. The nozzle pressure ratio and total temperature ratio are set to NPR = 3.514 and TTR = 3.2, respectively, at the inlet of the nozzle. The Mach number near the nozzle exit is $M_j = 1.469$, and the jet fully-expanded velocity is $u_j = 762.6$ m/s. The wall-adapting local eddy-viscosity (WALE) model by Nicoud et al. [28] is used as the sub-grid scale model. The shock detection algorithm of Persson [29] is used in conjunction with a modal exponential filter to stabilize the flow-field on a per element basis.

The flow-field variables, $\boldsymbol{q} = [\rho, u, v, w, p]$, from the simulation results can be decomposed as

$$\boldsymbol{q}(x, r, \theta, t) = \bar{\boldsymbol{q}}(x, r) + \boldsymbol{q}'(x, r, \theta, t), \tag{1}$$

where ρ is density, cylindrical coordinates (x, r, θ) with x-axis directed along the jet have corresponding velocities (u, v, w), p is pressure, t is time, $\bar{\boldsymbol{q}}(x, r)$ is the mean value defined as an average over the azimuthal direction and time, and $\boldsymbol{q}'$ is the flow variables perturbations.

The modulus and phase at each frequency ω_n and azimuthal mode number m can be obtained via computing the Fourier transform of the perturbation variables. We introduce the Fourier decomposition of flow variables as

$$\boldsymbol{q}'(x, r, \theta, t) = \sum_{n=-N_t/2}^{N_t/2-1} \sum_{m=-N_\theta/2}^{N_\theta/2-1} \hat{\boldsymbol{q}}_{mn}(x, r) \exp(i(m\theta - \omega_n t)), \tag{2}$$

where N_t is the total number of frequencies, N_θ is the total number of azimuthal modes, and $\hat{\boldsymbol{q}}_{mn}(x, r)$ is the Fourier coefficients. We will compare $\hat{\boldsymbol{q}}_{mn}(x, r)$ with the eigenfunctions from the instability wave solutions.

Far-field noise is calculated via the FWH equation, which uses flow-field information on an arbitrary shaped surface and the volume distribution of noise sources outside of the surface. The FWH equation is [30]

$$\left(\frac{1}{c_\infty^2}\frac{\partial^2}{\partial t^2} - \frac{\partial^2}{\partial x_i^2}\right) p' = \frac{\partial}{\partial t}[(\rho_\infty U_{\hat{n}})\delta(f)] - \frac{\partial}{\partial x_i}[L_i \delta(f)] + \frac{\partial^2}{\partial x_i \partial x_j}[T_{ij}\mathcal{H}(f)], \tag{3}$$

where c_∞ and ρ_∞ are the speed of sound and ambient density, $U_i = [1 - (\rho/\rho_\infty)]v_i + (\rho u_i/\rho_\infty)$, v_i are surface velocity components, u_i are the components of local fluid velocity, subscript $\hat{n}$ implies the dot product with unit surface normal vector, δ is the Dirac delta function, f is the function describing the FWH surface, $L_i = P_{ij}\hat{n}_j + \rho u_i(u_{\hat{n}} - v_{\hat{n}})$, $T_{ij} = \rho u_i u_j + (p' - c_\infty^2 \rho')\delta_{ij}$ is Lighthill's stress tensor, and $\mathcal{H}$ is the Heaviside function.

The equation is solved by Farassat [31] using a free-space Green's function of the wave equation for the condition that the surface is steady and no sources are outside of the surface. The solution is

$$p' = \frac{1}{4\pi}\int \left[\frac{\rho_\infty \dot{U}_{\hat{n}}}{r} + \frac{\dot{L}_r}{c_\infty r} + \frac{L_r}{r^2}\right]_{src} dS. \tag{4}$$

The integrand is evaluated at source time, where $r = |\boldsymbol{x} - \boldsymbol{y}|$ is the distance between the observer location $\boldsymbol{x}$ and the source location $\boldsymbol{y}$. The subscript r indicates the dot product with a unit vector in the observer direction. The $\dot{\square}$ indicates the time derivative.

B. Instability Wave theory

We review the main details of Tam's theory (see details [9, 10, 13]) because of its importance in this paper. We first examine the solution of a single instability wave, inner solution, outer solution, and matched asymptotic expansion method. We finally calculate the power spectrum of the instability wave by applying a stochastic theory.

1. Solution of Instability Waves

The small perturbation equations that govern the instability waves are derived from the linearized compressible, inviscid equations of motion in dimensionless form. The length, velocity, time, density, and pressure scales are the radius of the nozzle R_j, jet fully-expanded exit velocity u_j, R_j/u_j, the jet fully-expanded density at the nozzle exit ρ_j, and $\rho_j u_j^2$, respectively. The governing equations are

$$\frac{\partial \rho'}{\partial t} + \overline{\boldsymbol{V}} \cdot \nabla \rho' + \boldsymbol{V'} \cdot \nabla \bar{\rho} + \bar{\rho} \nabla \cdot \boldsymbol{V'} + \rho' \nabla \cdot \overline{\boldsymbol{V}} = 0, \tag{5}$$

$$\frac{\partial \boldsymbol{V'}}{\partial t} + \overline{\boldsymbol{V}} \cdot \nabla \boldsymbol{V'} + \boldsymbol{V'} \cdot \nabla \overline{\boldsymbol{V}} + \frac{\rho'}{\bar{\rho}} (\bar{V} \nabla \cdot \overline{\boldsymbol{V}}) = -\frac{1}{\bar{\rho}} \nabla p', \tag{6}$$

and

$$\frac{\partial p'}{\partial t} + \overline{\boldsymbol{V}} \cdot \nabla p' + \gamma \bar{p} \nabla \cdot \boldsymbol{V'} + \gamma p' \nabla \cdot \overline{\boldsymbol{V}} = 0, \tag{7}$$

where the prime denotes the perturbation, or a small-amplitude instability wave, $\overline{\boldsymbol{V}}$ is the mean velocity vector, and $\boldsymbol{V'}$ is the velocity perturbation vector. Equation (5) is the dimensionless continuity equation, Eqn. (6) is the dimensionless momentum equation, and Eqn. (7) is the dimensionless energy equation. The ideal gas law is used to close the equations.

The cylindrical coordinate system has its origin at the center of the nozzle exit. The term $\exp(im\theta - i\omega t)$ is separated from the solution because of the axial symmetry of the mean flow (azimuthal harmonics within round jets), and the assumption that the instability waves are generated by an external harmonic in time [32]. All the physical variables are represented in a form such as $p'(x, r, \theta, t) = \mathrm{Re}[p(x, r)\exp(im\theta - i\omega t)]$, where Re represents the real part. Equations (5) through (7) are now

$$-i\omega\rho + \bar{v}\frac{\partial \rho}{\partial r} + \bar{u}\frac{\partial \rho}{\partial x} + v\frac{\partial \bar{\rho}}{\partial r} + u\frac{\partial \bar{\rho}}{\partial x} + \bar{\rho}\left(\frac{1}{r}\frac{\partial vr}{\partial r} + \frac{im}{r}w + \frac{\partial u}{\partial x}\right) + \rho'\left(\frac{1}{r}\frac{\partial \bar{v}r}{\partial r} + \frac{\partial \bar{u}}{\partial x}\right) = 0, \tag{8}$$

$$-i\omega u + \bar{v}\frac{\partial u}{\partial r} + \bar{u}\frac{\partial u}{\partial x} + v\frac{\partial \bar{u}}{\partial r} + u\frac{\partial \bar{u}}{\partial x} = -\frac{1}{\bar{\rho}}\frac{\partial p}{\partial x}, \tag{9}$$

$$-i\omega v + \bar{v}\frac{\partial v}{\partial r} + \bar{u}\frac{\partial v}{\partial x} + v\frac{\partial \bar{v}}{\partial r} + u\frac{\partial \bar{v}}{\partial x} = -\frac{1}{\bar{\rho}}\frac{\partial \bar{p}}{\partial r}, \tag{10}$$

$$-i\omega w + \bar{v}\frac{\partial w}{\partial r} + \bar{u}\frac{\partial w}{\partial x} + 2\frac{\bar{v}w}{r} = -\frac{1}{r^2}\frac{im}{\bar{\rho}}p, \tag{11}$$

and

$$-i\omega p + \bar{v}\frac{\partial p}{\partial r} + \bar{u}\frac{\partial p}{\partial z} + \gamma\bar{p}\left(\frac{1}{r}\frac{\partial vr}{\partial r} + \frac{im}{r}w + \frac{\partial u}{\partial x}\right) + \gamma p\left(\frac{1}{r}\frac{\partial \bar{v}r}{\partial r} + \frac{\partial \bar{u}}{\partial x}\right) = 0. \tag{12}$$

Traditionally, these equations are solved via multiple scales analysis. Tam and Morris [14] showed that the multiple scales analysis is not valid far from the shear layer. Tam and Burton [9, 10] separated the jet flow into an inner and outer region to solve this problem. The corresponding mean flow is represented as

$$\overline{\boldsymbol{V}} = (\bar{u}(x, r), \epsilon\bar{v}(s, r), 0), r < r_m \tag{13}$$

and

$$\overline{\boldsymbol{V}} = (0, \epsilon\bar{v} = \epsilon\bar{v}_\infty/r, 0), r \geqslant r_m. \tag{14}$$

Equations (13) and (14) are the mean flow-field at the inner and outer region, where r_m is the boundary between the inner and outer region, and ϵ is the rate of spreading of the mixing layer, which is a small parameter.

The solution of Eqns. (8) to (12) can be expressed as an asymptotic series of waves traveling through a non-uniform medium, such as

$$p(s, r) = \sum_{n=0}^{\infty} \delta_n(\epsilon)\hat{p}_n(s, r)\exp\left[i\int_0^s \alpha(s)ds\right], \tag{15}$$

where $\delta_n(\epsilon)$ is the gauge function of the asymptotic expansion, the subscript n is order of the flow properties, $\hat{p}_n(s, r)$ is the shape function, and α is the local wavenumber.

In the inner region, the multiple scales analysis is used, and a slow variable $s = \epsilon x$ is introduced. Substituting ρ, u, v, w, and p in the form of Eqn. (15) into Eqns. (8) through (12), combining the mean flow in the inner region (Eqn. (13)), transforming the coordinate system (s, r), eliminating the term of $\exp\left[i\int_0^s \alpha(s)ds\right]$, rearranging equations according to the order n, and eliminating other dependent variables, the equation in terms of $\hat{p}_n$ for the n^{th} order is

$$\frac{\partial^2 \hat{p}_n}{\partial r^2} + \left[\frac{1}{r} + \frac{2}{\bar{\omega}}\frac{\partial \bar{u}}{\partial r} - \frac{1}{\bar{\rho}}\frac{\partial \bar{\rho}}{\partial r}\right]\frac{\partial \hat{p}_n}{\partial r} + \left[\bar{\rho}M_j^2\bar{\omega}^2 - \frac{m^2}{r^2} - \alpha^2\right]\hat{p}_n = G_n(r,s), \tag{16}$$

where $\bar{\omega} = \omega - \alpha\bar{u}$. The term G_n at the right side is only related to the lower order terms. When $n = 0$, the term G_n at the right side equals zero, namely, the equation becomes homogeneous and is called the Rayleigh equation, which is a simple differential equation relative to the pressure perturbation.

Equation (16) with appropriate boundary conditions forms an eigen-problem with given streamwise location, radial frequency, and azimuthal mode. To form a spatial stability analysis, ω is fixed, the eigenvalue is $\alpha = \alpha_r + i\alpha_i$, and the corresponding eigenfunction is $\hat{p}$. Some important properties of the eigenvalue and eigenfunction can be found as shown by Tam [13]. For example, if $\alpha = \alpha_r + i\alpha_i$ is an eigenvalue, then its complex conjugate $\alpha = \alpha_r - i\alpha_i$ is also an eigenvalue.

The solution of the Rayleigh equation can be expressed via the sum of two independent linear solutions, $\zeta_1^p(s,r)$ and $\zeta_2^p(s,r)$, as

$$\hat{p}_0(r,s) = A_0(s)\zeta_1^p(r,s) + B_0(s)\zeta_2^p(r,s), \tag{17}$$

where $A_0(s)$ and $B_0(s)$ are the amplitude functions varying in the streamwise direction. When r is close to r_m, the mean velocity is approximately zero. Thus, it requires $\zeta_1^p(r,s) \to H_m^{(1)}(i\lambda r)$. Here, $H_m^{(1)}(i\lambda r)$ is the m^{th} order of the first kind of Hankel function and $\lambda(\alpha) = (\alpha^2 - \bar{\rho}_\infty M_j^2\omega^2)^{1/2}$. The boundary condition for the jet centerline requires the solution to be finite as $r \to 0$. The amplitude functions will be determined later via the the method of matched asymptotic expansions after finding the outer solution.

In the outer region, multiple scales analysis is not valid because the perturbations have the same scale in each direction for the uniform condition. The Fourier transform method is used to solve for perturbation equations. An outer variable, $\bar{r} = \epsilon r$, is selected to ensure the same scale is obtained with the variable s. We repeat the procedure for solving the inner solution except combining the mean flow in the outer region (Eqn. (14)), and perform the Fourier transform on the variable s. The final equation is

$$\left[1 - \epsilon^4\bar{\rho}_\infty M_j^2\frac{\bar{v}_\infty^2}{\bar{r}^2}\right]\frac{\partial^2\tilde{u}}{\partial\bar{r}^2} + \left[\frac{1}{\bar{r}} + i\epsilon 2\bar{\rho}_\infty M_j^2\bar{\omega}_k\frac{\bar{v}_\infty}{\bar{r}} + \epsilon^4\bar{\rho}_\infty M_j^2\frac{\bar{v}_\infty^2}{\bar{r}^3}\right]\frac{\partial\tilde{u}}{\partial\bar{r}} + \left[\bar{\rho}_\infty M_j^2\frac{\bar{\omega}_\infty^2}{\epsilon^2} - \frac{m^2}{\bar{r}^2} - k^2\right]\tilde{u} = 0, \tag{18}$$

where $\tilde{u}$ is the Fourier transform of u. Based on the relations between the dependent variables and inverse Fourier transform [13], the solution in terms of pressure at the outer region is

$$p(\bar{r},s) = \int_{-\infty}^{\infty} g(k,\epsilon)\left[1 + i\frac{\epsilon^3}{\bar{\omega}_k}\frac{\bar{v}_\infty}{\bar{r}}\frac{\partial}{\partial\bar{r}}\right]\left\{\left(\bar{r}^2 - \epsilon^4\bar{\rho}_\infty^2 M^2\omega^2\bar{v}_\infty^2\right)^{-1/2i\epsilon^2\bar{\rho}_\infty M_j^2\bar{\omega}_k\bar{v}_\infty}\right.$$
$$\left.\times H_q^1\left(\frac{1}{i\epsilon}(\epsilon^2k^2 - \bar{\rho}_\infty M_j^2\bar{\omega}_k^2)^{1/2}\right)\left(\bar{r}^2 - \epsilon^4\bar{\rho}_\infty^2 M_j^2\bar{v}_\infty^2\right)\right\}e^{iks}dk, \tag{19}$$

where $g(k,\epsilon) = \frac{1}{2\pi}\int_{-\infty}^{\infty}\tilde{A}(s)e^{i\int_0^x\alpha(x;\omega,m)dx - iks}dk$ and $\tilde{A}(s)$ is the amplitude function.

There is an overlapping region where the inner and outer solution are both valid. Therefore, the method of matched asymptotic expansions is applied [10, 11]. Firstly, the intermediate variables $\bar{r} = r\epsilon^{1/N}$ (N is a large positive number) and a variable transformation $\eta = k\epsilon$ are introduced. We apply the intermediate matching procedure, which involves expanding the inner solution and outer solution in terms of the intermediate variables until the difference between the two solutions vanish [11]. After expanding the two solutions for both the order unity and the higher order, the relations and values of the amplitude function are derived, $\tilde{A}_0(s) = A_0(s)$, $B_0(s) = 0$, and $A_0(s) = \hat{A}_0\exp[-\beta(s)]$. $\beta(s) = \int_0^s I_2/I_1 ds$ is the non-parallel flow correction factor, I_1 and I_2 are two complex integral terms, and $\hat{A}_0$ is the amplitude of the instability wave at the nozzle exit plane.

To summarize, the inner solution and outer solution of zeroth order, in terms of pressure p, at the given radial frequency and azimuthal mode number are

$$p_0^{\text{inner}}(x,r,\theta,t;\omega,m) = A_0(x;\omega,m)\zeta_1^p(r,x;\omega,m)\exp\left[i\int_0^x \alpha(x;\omega,m)dx + m\theta - \omega t + (\pi/2)\right], \tag{20}$$

$$p_0^{\text{outer}}(x,r,\phi,t;\omega,m) = \int_{-\infty}^{\infty} \hat{A}_0(\omega,m)\hat{g}(\eta;\omega,m)H_m^{(1)}[i\lambda(\eta)r]\exp\{i[\eta x + m\theta - \omega t + (\pi/2)]\}d\eta, \tag{21}$$

and

$$\hat{g}(\eta;\omega,m) = \frac{1}{2\pi}\int_{-\infty}^{\infty}\exp\left\{\left[i\int_0^x \alpha(x;\omega,m)dx - \eta x\right] - \beta(x;\omega,m)\right\}dx, \tag{22}$$

where $\hat{g}(\eta;\omega,m)$ is the wavenumber spectrum. The properties of β and $\hat{g}$ can be found (see Tam [13]).

2. Formation of the Stochastic Instability Wave

The model contains an unknown initial wave amplitude $\hat{A}_0(\omega,m)$. It is set as a stochastic random function to represent the random character of large-scale turbulent structures. The normalized amplitude $a(\omega,m)$ of $\hat{A}_0(\omega,m)$ is defined as

$$\hat{A}_0(\omega,m) = \frac{a(\omega,m)}{|\zeta_1^p(0,r_{1/2},;\omega,m)|}, \tag{23}$$

where $|\zeta_1^p(r_{1/2},0;\omega,m)|$ is the amplitude of the pressure eigenfunction at the half-velocity of the nozzle exit plane.

The auto-correlation function $|\zeta_1^p(0,r_{1/2};\omega,m)|$ has the form of a product of delta functions because we assume that the instability wave spectrum is initiated by the white noise. That is, the total pressure associated with instability waves can be represented by the form of the product of the delta function. The total inner pressure perturbations $p(x,r,\theta,t)$ are obtained by summing all the instability waves at each radial frequency and azimuthal mode, the ensemble average is from Tam [13]

$$\left\langle p(0,r_{1/2},\theta,t), p(0,r_{1/2},\theta+\Theta,t+\tau)\right\rangle = \sum_{n=-\infty}^{\infty}\sum_{n=-\infty}^{\infty}\int\int_{-\infty}^{\infty}\frac{\langle a(\omega,m),a(\omega',m')\rangle\,\zeta_1^p(0,r_{1/2};\omega,m)\zeta_1^p(0,r_{1/2};\omega',m')}{|\zeta_1^p(0,r_{1/2};\omega,m)||\zeta_1^p(0,r_{1/2},;\omega',m')|}$$
$$\exp\{i\left[(m+m')\,\phi - (\omega+\omega')\,t + m\theta - \omega\tau + \pi\right]\}d\omega d\omega' = 2\pi^2\tilde{D}\delta(\Theta)\delta(\tau), \tag{24}$$

where < > denotes ensemble average, Θ is phase lag, τ is retarded time, and $\tilde{D}$ is the area of the auto-correlation function, which is the only unknown parameter.

The ensemble average of the normalized amplitude function is

$$\langle a(\omega,m),a(\omega',m')\rangle = (\tilde{D}/2)\delta(\omega+\omega')\delta_{m,-m'}, \tag{25}$$

where $\delta_{m,-m'}$ is Kronecker delta function.

Similarly, the total pressure perturbation outside the jet are obtained by summing Eqn. (21) at each radial frequency and azimuthal mode. The power spectrum $S(x,r,\theta,\omega)$ of the acoustic pressure is the Fourier transform of the autocorrelation function of the total outer pressure perturbation. The procedure is outlined by Tam [13] and results in

$$S(x,r,\theta,\omega) = \frac{1}{2\pi}\int_{-\infty}^{\infty}\langle p(x,r,\theta,t),p(x,r,\theta,t+\tau)\rangle\exp(-i\omega\tau)d\tau = (\tilde{D}/2)\sum_{m=-\infty}^{\infty}\frac{|G(x,r;\omega,m)|^2}{|\zeta_1^p(0,r_{1/2};\omega,m)|^2}. \tag{26}$$

and

$$G(x,r;\omega,m) = \int_{-\infty}^{\infty}\hat{g}(\eta;\omega,m)H_m^{(1)}[i\lambda(\eta)r]\exp(-i\eta x)d\eta. \tag{27}$$

By transforming the cylindrical coordinate system to a spherical coordinate system, $x = R\cos\psi$ and $r = R\sin\psi$, and applying the stationary phase approximation method to evaluate G at large R [13], Eqn. (26) is simplified to

$$\tilde{S}(R,\phi,\psi,f) = 10\log_{10}\left[\frac{\rho_j^2 u_j^3 R_j^3}{p_{\text{ref}}^2 R^2}\sum_{m=-\infty}^{\infty}\frac{8\pi\tilde{D}|\hat{g}(\bar{\eta};\omega,m)|^2}{|\zeta_1^p(0,r_{1/2};\omega,m)|}\right], \tag{28}$$

where $\tilde{S}$ is the noise power spectrum in decibels, $f(\omega = 2\pi f)$ is frequency, $p_{\text{ref}} = 2\times10^{-5}$ Pa is the reference pressure, $\bar{\eta} = \bar{\eta}(\psi)$ is the stationary phase, and limiting $0^\circ \le \psi \le 180^\circ$ denotes the direction from the upstream nozzle centerline axis. The expression of $\bar{\eta}$ can be found from Dahl [11] or Tam [10].

III. Results and Analysis

In this section, we examine the results of jet noise predicted by instability wave theory and LES. Stability properties, amplification rates, and mode shapes from LES are compared with the instability wave predictions at particular frequencies. The far-field sound pressure level (SPL) predicted with instability wave theory and LES are compared with measurements of the SHJAR database. In addition, the SPL at different azimuthal modes are shown.

A. LES Data Analysis

Figure 1 shows the results of mean axial velocity and the turbulent kinetic energy (TKE) along the jet centerline. The LES results are compared with an axisymmetric RANS simulation with the same jet operating condition. Figure 1(a) shows that both simulations have similar shock-cell structures. The amplitude of the mean axial velocity from LES only has a small difference compared to RANS from the nozzle exit to $x/D = 7$. The mean axial velocity decays at a slower rate in RANS relative to the LES after $x/D = 7$. Similar decay between LES and RANS are observed by Georgiadis et al. [33]. The potential core length of LES is approximately $7.5D$. Both simulations capture a similar overall trend of TKE variations as observed in Fig. 1(b), while LES predicts a higher maximum value. TKE of LES is modulated due to the shock cell structure.

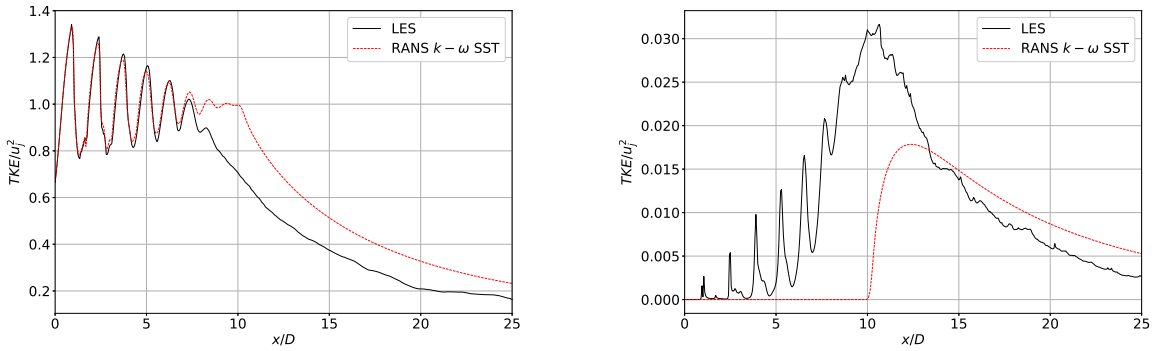

(a) Mean axial velocity distribution

(b) TKE

Fig. 1 Comparison of mean axial velocity distribution and TKE between the LES and RANS simulation on the centerline.

An instantaneous pressure field of the LES is shown in Fig. 2. At the nozzle exit, semi-periodic shock-cells are formed due to pressure mismatch between the nozzle exhaust and ambient gas. The pressure in the near-field is dominated by downstream propagating acoustic waves. Mach wave radiation propagating downstream with parallel patterns is observed. BBSAN and screech tone noise propagate in the upstream direction, which is caused by the unsteady interaction between the shock cell structures and the instability waves.

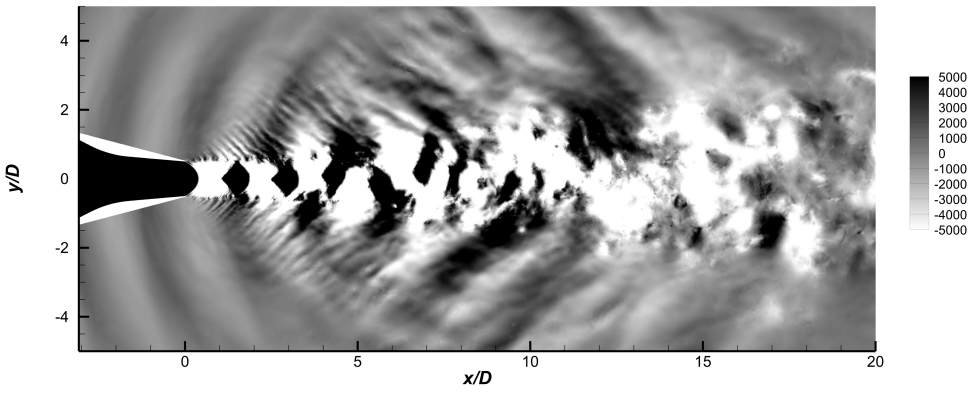

Fig. 2 Instantaneous pressure contour $(p - p_\infty)$ in Pa.

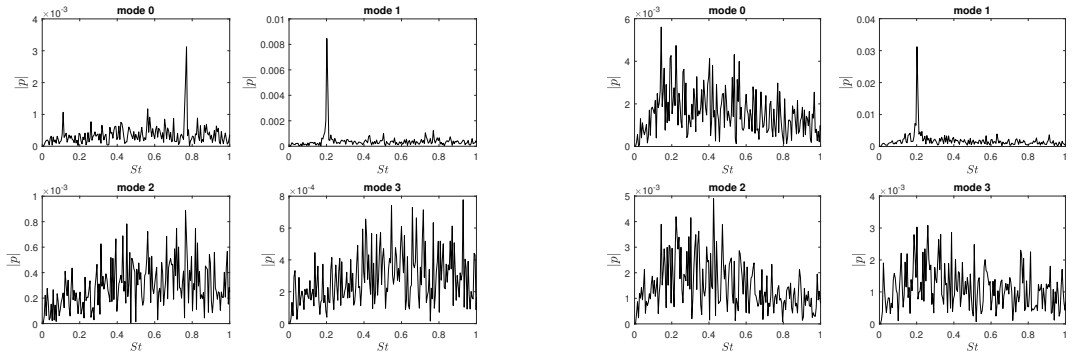

(a) $x/D = 1$

(b) $x/D = 4$

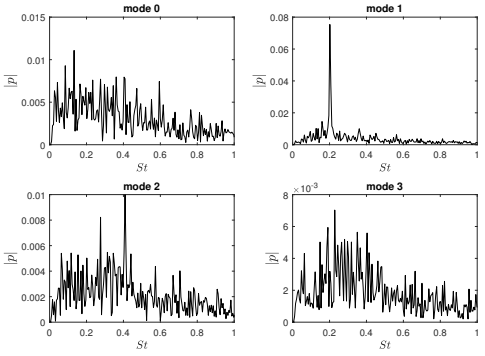

(c) $x/D = 7$

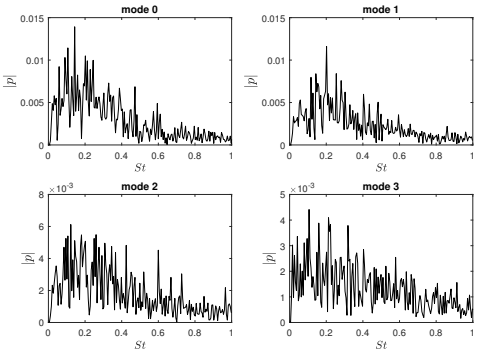

(d) $x/D = 10$

Fig. 3 Frequency spectra of modal pressure perturbations of LES data at several axial positions in the jet shear layer at $r/D = 0.5$.

Frequency spectra of pressure perturbations of the LES data inside the shear layer at $r/D = 0.5$ and axial locations $x/D = 1, 4, 7$, and 10 for azimuthal modes $m = 0$ to 3 are shown in Fig. 3. The frequency spectra is dominated by the intermediate frequencies near $St = 0.2$ at mode 1 for different axial locations, which are especially apparent at the

$x/D = 1$ location. There is a clear energy transfer to lower frequencies as the probes move downstream. For example, the amplitude of pressure spectra at $x/D = 10$ is higher than that of $x/D = 4$ and 7 at mode 0 for lower frequencies as shown in the Fig. 3(b), 3(c), and 3(d).

These results are representative of the pressure fluctuations at all frequencies. It is difficult to detect the effects of instability waves within these results. Therefore, it is necessary to examine specific frequencies for particular linear instability modes. These instability modes will correlate with sound radiated from the shear layer in the direction of the dominant radiation direction (see Mohseni [15]).

For this jet, the screech tone occurs at $St = 0.20$ as observed in the Fig. 3, and the feed-back mechanism instigates strong instability waves at this particular frequency and its harmonics [1]. It is these frequencies that are most amplified in LES that can also be accurately predicted by instability wave theory. Therefore, we will choose $St = 0.2006$, $St = 0.1003$ the subharmonic frequency of $St = 0.2006$, and $St = 0.4004$ which is close to the harmonic frequency of $St = 0.2006$.

B. Instability Wave Detection

1. Stability Analysis

We seek to ascertain the instability wave solution. First, we find the local wavenumber by solving the eigenvalue problem defined in the Rayleigh equation. The phase speed and axial growth rate of the instability wave are obtained from the complex wave number α=α_r+$i\alpha_i$. The real part of the complex wave number represents the number of axial oscillations per unit of space (axial wave number), and the phase speed is obtained from u_p=$\omega\alpha_r^{-1}$=$\pi St\alpha_r^{-1}$ [34]. The phase speed provides a measure of the convection speed of the instability wave. The growth rate is given by $-\alpha_i$. If the growth rate is positive, then the instability wave is amplified, whereas, the instability wave becomes damped if the growth rate is negative. In general, the growth rate of the instability wave will decrease as the jet shear layer becomes thicker, and further downstream, it becomes damped.

There are two main methods to solve the Rayleigh equation. One is the shooting method, and the other is the global or direct method [17, 35]. The latter method discretizes the equation via the finite difference [11] or spectral approach [36] and transforms the problem to a linear algebra equation. A bi-global method was also proposed to account for the effect of serrated nozzles [34]. In this study, the global method via central finite differencing developed by Dahl [11] is adapted. The mean velocity and density within the Rayleigh equation are adapted from LES. Figure 4 shows the radial velocity and radial density at different axial positions. It can be seen that the velocity will decay sharply outside the jet in the core region. At the end of the core and the transitional regions, it is observed that the mean streamwise velocity slowly spreads. This trend is also observed for density.

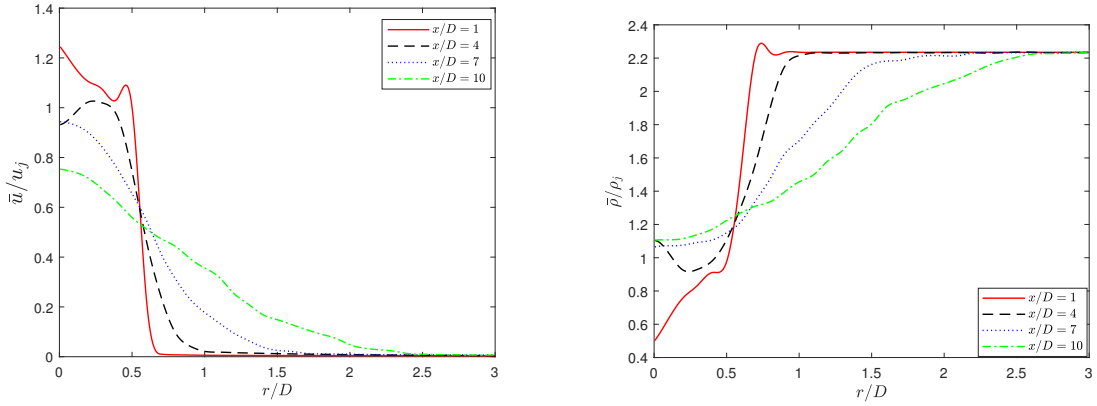

(a) Radial velocity distribution

(b) Radial density distribution

Fig. 4 Variation of the streamwise velocity component and density in the radial direction at different axial locations from the LES.

Figure 5 presents the phase speed and growth rate for $0 < St < 0.6$ at $\Delta St = 0.05$ for different azimuthal modes at $x/D = 2.5$. For different azimuthal modes, the phase speeds have similar trends, at first decreasing and then increasing

a little. Generally, the growth rate is relatively small at lower and higher St, with peaks near $St \sim 0.2$. The growth rate of mode 0 is lower than mode 1 and mode 2.

Figure 6 shows the phase speed and growth rate in the streamwise direction at $St = 0.2006$ for modes 0, 1, and 2. The analysis is initiated from $x/D = 0.1$, which is the left boundary of the sampling region of the LES. The phase speeds exhibit strong oscillations inside the potential core region for all modes analyzed, after which phase speeds begin to decay sharply. This phenomenon reflects that the instability wave extracts the energy from the mean flow and is similar to the mean flow variation in the core region. The phase speed of mode 0 is larger than other modes inside the potential core region. The initial growth rates for all modes peak on the initial axial plane and then decay with axial distance. However, the growth rates appear to contain a local increase near $x/D = 2$. The growth rate of mode 0 is smaller than the other two modes. The instability wave of modes 0 and 2 are damped or saturated earlier in the streamwise direction relative to mode 1.

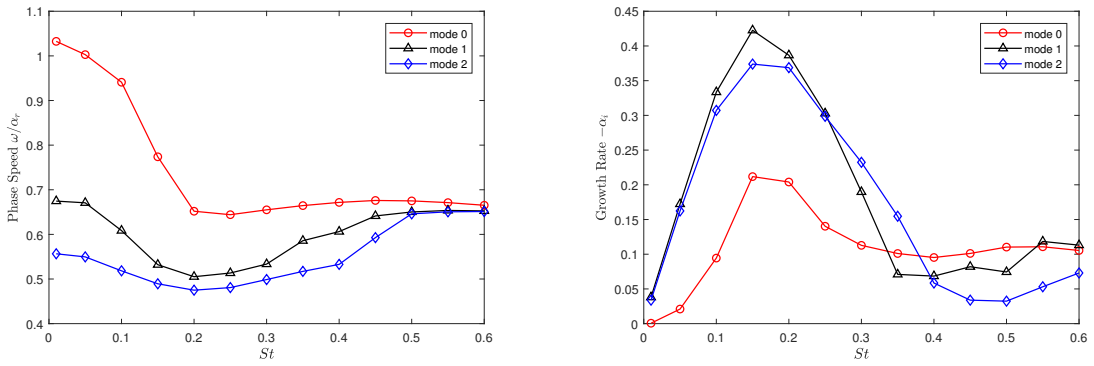

(a) Phase speed (b) Growth rate

Fig. 5 Variation of phase speed and growth rate of different azimuthal modes at $x/D = 2.5$.

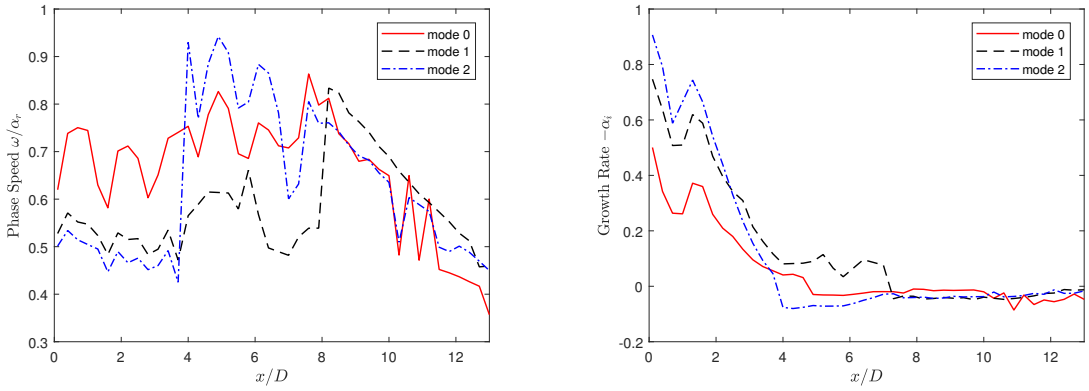

(a) phase speed (b) Growth rate

Fig. 6 The development of phase speed and growth rate of different azimuthal modes along the streamwise direction at $St = 0.2006$.

2. Eigenfunction comparison

The shape function $\hat{\boldsymbol{q}}$ is important for determining the spatial distribution of perturbations. Figures 7 and 8 show comparisons of the shape functions of pressure and axial velocity perturbations at different axial locations for mode 0 and mode 1 between the LES and instability wave solution. The corresponding St is 0.2006. The eigenfunctions are not

valid at larger r because solutions of the compressible Rayleigh equation must be asymptotically matched with the outer solution. For this reason, the shape functions at a specified axial location are scaled with the maximum value obtained from LES at equivalent axial locations. For mode 0, the eigenfunction can be matched at the lip-line when $x/D < 2.5$, while the agreement is poor in the region $2.5 < x/D < 6$. That is because the instability wave excited by the screech tone is amplified and interacts with the shock cell structure. The instability wave theory cannot capture the nonlinear effects. The corresponding eigenfunctions of axial velocities have large values due to the existence of a critical layer. Similar trends are observed for mode 1.

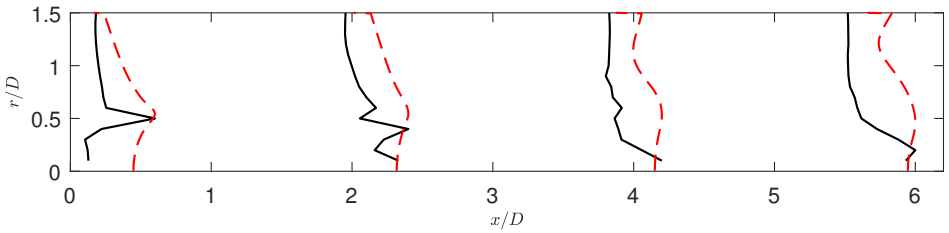

(a) Pressure eigenfunctions

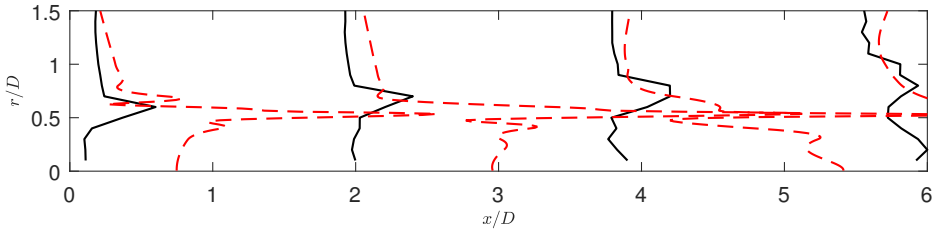

(b) Axial velocity eigenfunctions

Fig. 7 Comparisons of pressure and axial velocity eigenfunctions for mode 0 between LES (———) and prediction (– – –).

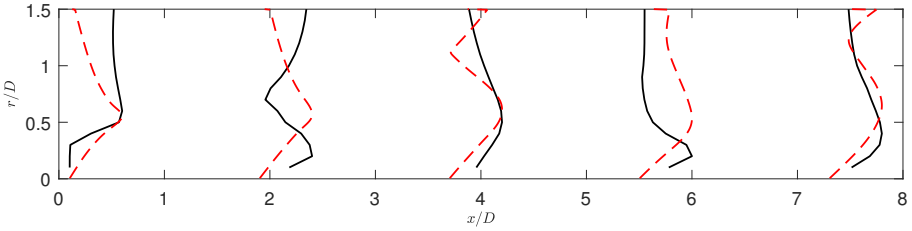

(a) Pressure eigenfunctions

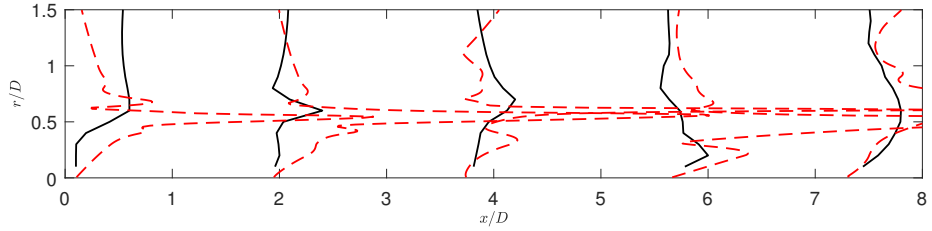

(b) Axial velocity eigenfunctions

Fig. 8 Comparisons of pressure and axial velocity eigenfunctions for mode 1 between LES (———) and prediction (– – –).

The amplitudes of the instability waves are an important factor for determining the radiated jet noise. We examine

the radial location of $r/D = 0.5$, where the effects of the instability waves on noise are significant. Figure 9 shows the comparisons of the pressure perturbations along the streamwise direction at $St = 0.2006$ for mode 0 and mode 1. In order to compare predictions with the LES, the amplitude of the instability waves are normalized with LES at $x/D = 0.1$. The peak locations of pressure perturbations are shifted upstream for the instability wave solution for mode 0. The largest amplitudes for LES appear in the fully developed region. Strong Mach wave radiation can influence the linear hydrodynamic region, and this may be contributing to the discrepancy. The instability wave solutions agree with LES relative to mode 1. Larger perturbations are located within the potential core region of the shear layer. The instability wave pressure perturbations and LES both decay after the core region. The decay rate of the perturbation of the instability wave is higher due to the collapse of large-scale coherent structures after the potential core region.

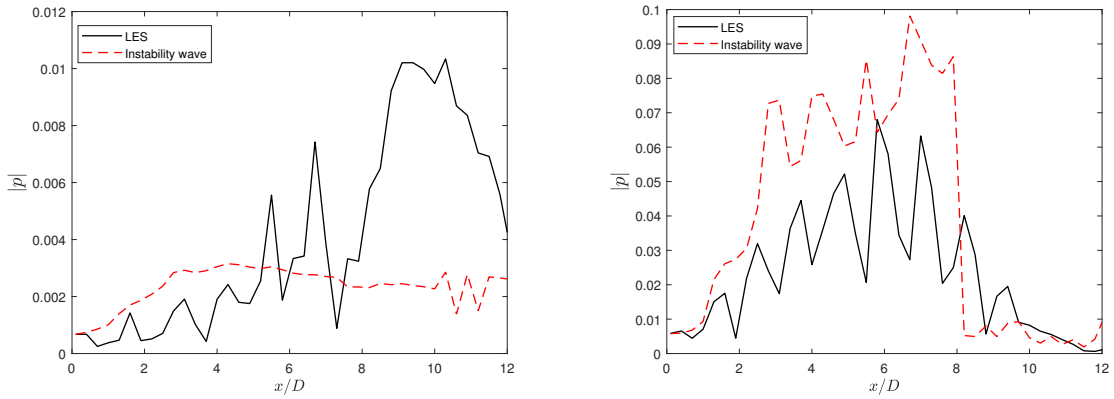

(a) Mode 0 (b) Mode 1

Fig. 9 Comparisons of pressure perturbations between LES (———) and prediction (– – –) for mode 0 and mode 1 in the shear layer $r/D = 0.5$.

C. Far-field Sound in Supersonic jets

The far-field SPL from the instability wave solution is evaluated by Eqn. (28), where the term $\hat{g}(\bar{\eta}; \omega, m)$ is complex due to the non-parallel flow correction factor β. For simplicity, setting this term to zero results in $\hat{g}$ being the Fourier transform of the instability wave. The axial source region is chosen to extend to $x = 13D$, which is the maximum downstream location we sampled LES data.

Figure 10 shows the computed far-field SPL at $St = 0.1003$, $St = 0.2006$, and $St = 0.4004$. The unknown constant $\tilde{D}$ in the Eqn. (28) is set equal to 0.05, which ensures the SPL is same as the maximum of experiment measurements at $St = 0.2006$. Figure 10(b) shows that predicted SPL matches experiment measurements for $\psi < 80°$, where the jet noise from the large-scale turbulence dominants. In the upstream direction, the predicted SPL is approximately 7-10 dB lower than measurements. Our predictions confirm that the instability waves radiate noise in the upstream direction, but this noise is dominated by fine-scale mixing noise and BBSAN. For LES predictions, the peak noise amplitude in the upstream direction is dominated by BBSAN. The SPL predicted by LES differs by at most 4 dB relative to experiment over the whole region as shown in Figs. 10(a) and 10(b). The predicted SPL of the instability wave at $St = 0.4004$ in Fig. 10(c) is smaller than experimental measurements and LES both in the upstream and downstream directions. For the subharmonic frequency of the excited instability wave in Fig. 10(a) shows that predicted SPL is 5-8 dB lower than the experiment in the downstream direction. This is because nonlinear effects are more pronounced at lower frequencies.

Figure 11 illustrates comparisons between the LES and instability wave theory at different azimuthal modes. We only present the positive azimuthal modes. The negative modes will result in the same predictions as positive modes. The SPL of LES at mode 0 is higher than the other modes, which means large-scale turbulent structures contribute more to mode 0 radiated acoustic energy in the downstream direction. Mode 1 contains the dominant instability noise. According to Tam [1], when $M_j > 1.3$ the screech tone will change the mode shape from axisymmetric (mode 0) to helical (mode 1). Our predictions capture this observation. In the near field at $St = 0.2006$, the amplitude of pressure perturbations of instability waves for mode 1 are larger than mode 0, and this property is retained in the far-field. For $St = 0.4004$, the SPL of instability wave theory at mode 2 and 3 is larger than mode 0 and 1, which means that the

dominant modes will change or there is no single dominant mode for higher frequencies as described by Tam [13].

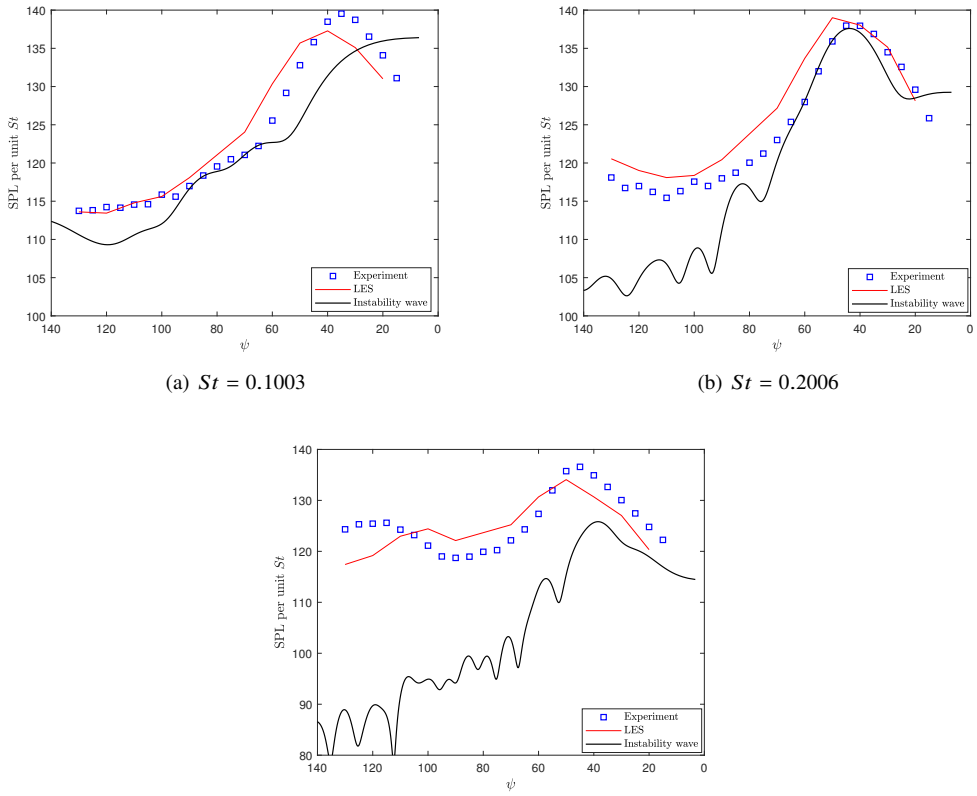

(a) St = 0.1003

(b) St = 0.2006

(c) St = 0.4004

Fig. 10 Far-field noise comparisons on a polar arc of 100D relative to the nozzle exit at different St.

IV. Summary and Conclusion

We predicted the aerodynamics and radiated jet noise in the acoustic far-field for an under-expanded heated supersonic jet via LES and the instability wave theory of Tam [9, 10, 13]. The mean flow-field and TKE of LES show good agreement with the RANS prediction and previous investigations. The radiated noise of LES predicted by the FWH equation shows excellent agreement with the measurements of Brown and Bridges [19]. The instability wave theory captures the directivity pattern of large-scale turbulent structures in the dominant radiation direction. Instability theory also is able to quantify the radiation of noise from large-scale structures in the upstream radiation direction. Predicted phase speed in the streamwise direction oscillates strongly with mean flow variations due to the existence of the shock cell structure. Similarly, the pressure perturbation from LES and instability wave theory oscillates in the core region at the dominant frequency of mode 1. Predictions using instability wave theory show that the screech tone can alter the dominant mode shape of jet noise from the axisymmetric to helical mode.

The shape functions of instability waves and LES match well in part of the amplifying region in the streamwise direction. The azimuthal mode components of radiated jet noise in the far-field do not match well with LES, especially for mode 0. These results demonstrate that the turbulent structures and sound generation mechanisms are more complex in under-expanded heated jets relative to on-design jets. More advanced methods to extract the large-scale turbulent structures are necessary. There are limitations of the presently investigated linear instability wave theory. The amplitude of the instability wave needs to be calibrated by extracting the large scale turbulent structures from LES. The nonlinear interactions mechanism at the lower frequencies cannot be accounted for in linear theory.

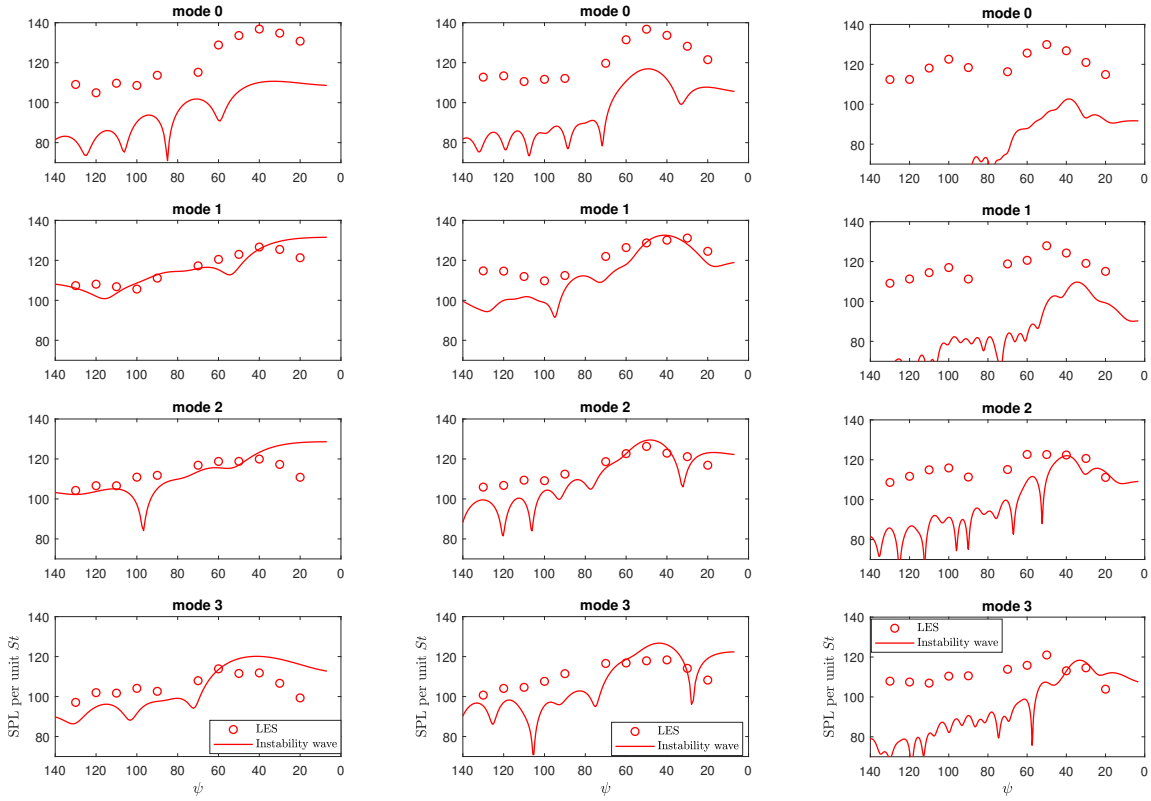

(a) $St = 0.1003$ (b) $St = 0.2006$ (c) $St = 0.4004$

Fig. 11 Far-field noise comparisons on a polar arc of 100D at different St at different azimuthal modes.

Acknowledgments

The first author is supported by SERDP WP19-1014 SERDP/ESTCP under program manager Robin Nissan. The second author is supported by the Office of Naval Research Grant N00014-17-1-2583 under program manager Steven Martens. Any opinions, findings, and conclusions or recommendations expressed in this material are those of the author(s) and do not necessarily reflect the views of the Office of Naval Research.

References

[1] Tam, C. K. W., "Supersonic Jet Noise," *Annual Review of Fluid Mechanics*, Vol. 27, No. 1, 1995, pp. 17–43. doi:10.1146/annurev.fl.27.010195.000313.

[2] Tam, C. K. W., Golebiowski, M., and Seiner, J., "On the Two Components of Turbulent Mixing Noise from Supersonic Jets," *Aeroacoustics Conference*, AIAA Paper No. 1996-1716, 1996. doi:10.2514/6.1996-1716.

[3] Lighthill, M. J., "On Sound Generated Aerodynamically I. General Theory," *Proceedings of the Royal Society of London. Series A. Mathematical and Physical Sciences*, Vol. 211, No. 1107, 1952, pp. 564–587. doi:10.1098/rspa.1952.0060.

[4] Ffowcs-Williams, J. E., "The Noise from Turbulence Convected at High Speed," *Philosophical Transactions of the Royal Society A: Mathematical, Physical and Engineering Sciences*, Vol. 255, No. 1061, 1963, pp. 469–503. doi:10.1098/rsta.1963.0010.

[5] Lilley, G. M., "On the Noise from Jets. In Noise Mechanism," *Annual Review of Fluid Mechanics*, Vol. 131, No. 345, 1974, pp. 13.1–13.12.

[6] Goldstein, M. E., "Aeroacoustics of Turbulent Shear Flows," *Annual Review of Fluid Mechanics*, Vol. 16, No. 1, 1984, pp. 263–285. doi:10.1146/annurev.fl.16.010184.001403.

[7] Miller, S. A. E., "Toward a Comprehensive Model of Jet Noise Using an Acoustic Analogy," *AIAA Journal*, Vol. 52, No. 10, 2014, pp. 2143–2164. doi:10.2514/1.j052809.

[8] Tam, C. K. W., and Morris, P. J., "The Radiation of Sound by the Instability Waves of a Compressible Plane Turbulent Shear Layer," *Journal of Fluid Mechanics*, Vol. 98, No. 2, 1980, pp. 349–381. doi:10.1017/s0022112080000195.

[9] Tam, C. K. W., and Burton, D. E., "Sound Generated by Instability Waves of Supersonic Flows. Part 1. Two-dimensional Mixing Layers," *Journal of Fluid Mechanics*, Vol. 138, No. -1, 1984, p. 249. doi:10.1017/s0022112084000112.

[10] Tam, C. K. W., and Burton, D. E., "Sound Generated by Instability Waves of Supersonic Flows. Part 2. Axisymmetric Jets," *Journal of Fluid Mechanics*, Vol. 138, No. -1, 1984, p. 273. doi:10.1017/s0022112084000124.

[11] D. Dahl, M., "The Aeroacoustics of Supersonic Coaxial Jets," Ph.D. thesis, The Pennsylvania State University, Dec 1994.

[12] Tam, C. K. W., and Hu, F. Q., "On the Three Families of Instability Waves of High-speed Jets," *Journal of Fluid Mechanics*, Vol. 201, No. 1, 1989, p. 447. doi:10.1017/s002211208900100x.

[13] Tam, C. K. W., and Chen, P., "Turbulent Mixing Noise from Supersonic Jets," *AIAA Journal*, Vol. 32, No. 9, 1994, pp. 1774–1780. doi:10.2514/3.12173.

[14] Tam, C. K. W., and Chen, K. C., "A Statistical Model of Turbulence in Two-dimensional Mixing Layers," *Journal of Fluid Mechanics*, Vol. 92, No. 2, 1979, pp. 303–326. doi:10.1017/S002211207900063X.

[15] Mohseni, K., "A. Universality in Vortex Formation. B. Evaluation of Mach Wave Radiation in a Supersonic Jet," Ph.D. thesis, California Institute of Technology, Nov 2000.

[16] Ryu, J., and Lele, S. K., "Instability Waves in High-Speed Jets: Near-and Far-Field DNS/LES Data Analysis," *International Journal of Aeroacoustics*, Vol. 14, No. 3-4, 2015, pp. 643–673. doi:10.1260/1475-472x.14.3-4.643.

[17] Gudmundsson, K., "Instability Wave Models of Turbulent Jets from Round and Serrated Nozzles," Ph.D. thesis, California Institute of Technology, Jan 2010.

[18] Suzuki, T., and Colonius, T., "Identification of Jet Instability Waves and Design of a Microphone Array," *10th AIAA/CEAS Aeroacoustics Conference*, AIAA Paper No. 2004-2960, 2004. doi:10.2514/6.2004-2960.

[19] Brown, C., and Bridges, J., "Small Hot Jet Acoustic Rig Validation," NASA TM-2006-214234, April 2006.

[20] López, M. R., Sheshadri, A., Bull, J. R., Economon, T. D., Romero, J., Watkins, J. E., Williams, D. M., Palacios, F., Jameson, A., and Manosalvas, D. E., "Verification and Validation of HiFiLES: a High-Order LES Unstructured Solver on Multi-GPU Platforms," *32nd AIAA Applied Aerodynamics Conference*, AIAA Paper No. 2014-3168, 2014. doi:10.2514/6.2014-3168.

[21] Vincent, P. E., Castonguay, P., and Jameson, A., "A New Class of High-order Energy Stable Flux Reconstruction Schemes," *Journal of Scientific Computing*, Vol. 47, No. 1, 2011, pp. 50–72. doi:10.1007/s10915-010-9420-z.

[22] Hesthaven, J. S., and Warburton, T., *Nodal Discontinuous Galerkin Methods: Algorithms, Analysis, and Applications*, Springer Science & Business Media, 2007.

[23] May, G., and Jameson, A., "A Spectral Difference Method for the Euler and Navier-Stokes Equations on Unstructured Meshes," *44th AIAA Aerospace Sciences Meeting and Exhibit*, AIAA Paper No. 2006-304, 2006. doi:10.2514/6.2006-304.

[24] Toro, E. F., *Riemann Solvers and Numerical Methods for Fluid Dynamics: a Practical Introduction*, Springer Science & Business Media, 2013.

[25] Huynh, H. T., "A Flux Reconstruction Approach to High-Order Schemes Including Discontinuous Galerkin Methods," *18th AIAA Computational Fluid Dynamics Conference*, AIAA Paper No. 2007-4079, 2007. doi:10.2514/6.2007-4079.

[26] Huynh, H. T., "A Reconstruction Approach to High-Order Schemes Including Discontinuous Galerkin for Diffusion," *47th AIAA Aerospace Sciences Meeting including The New Horizons Forum and Aerospace Exposition*, AIAA Paper No. 2009-403, 2009. doi:10.2514/6.2009-403.

[27] Castonguay, P., Vincent, P. E., and Jameson, A., "A New Class of High-Order Energy Stable Flux Reconstruction Schemes for Triangular Elements," *Journal of Scientific Computing*, Vol. 51, No. 1, 2012, pp. 224–256. doi:10.1007/s10915-011-9505-3.

[28] Nicoud, F., and Ducros, F., "Subgrid-scale Stress Modelling Based on the Square of the Velocity Gradient Tensor," *Flow, Turbulence and Combustion*, Vol. 62, No. 3, 1999, pp. 183–200. doi:10.1023/A:1009995426001.

[29] Persson, P. O., "Shock Capturing for High-Order Discontinuous Galerkin Simulation of Transient Flow Problems," *21st AIAA Computational Fluid Dynamics Conference*, AIAA Paper No. 2013-3061, 2013. doi:10.2514/6.2013-3061.

[30] Brentner, K. S., and Farassat, F., "Analytical Comparison of the Acoustic Analogy and Kirchhoff Formulation for Moving Surfaces," *AIAA Journal*, Vol. 36, No. 8, 1998, pp. 1379–1386. doi:10.2514/2.558.

[31] Farassat, F., "Derivation of Formulations 1 and 1A of Farassat," 2007. NASA/TM-2007-214853.

[32] Kopiev, V., Chernyshev, S., Zaitsev, M., and Kuznetsov, V., "Experimental Validation of Instability Wave Theory for Round Supersonic Jet," *12th AIAA/CEAS Aeroacoustics Conference (27th AIAA Aeroacoustics Conference)*, AIAA Paper No. 2006-2595, 2006. doi:10.2514/6.2006-2595.

[33] Georgiadis, N. J., Yoder, D. A., and Engblom, W. B., "Evaluation of Modified Two-Equation Turbulence Models for Jet Flow Predictions," *AIAA Journal*, Vol. 44, No. 12, 2006, pp. 3107–3114. doi:10.2514/1.22650.

[34] Uzun, A., Alvi, F. S., Colonius, T., and Hussaini, M. Y., "Spatial Stability Analysis of Subsonic Jets Modified for Low-Frequency Noise Reduction," *AIAA Journal*, Vol. 53, No. 8, 2015, pp. 2335–2358. doi:10.2514/1.J053719.

[35] Morris, P. J., "The Instability of High Speed Jets," *International Journal of Aeroacoustics*, Vol. 9, No. 1-2, 2010, pp. 1–50. doi:10.1260/1475-472x.9.1-2.1.

[36] Liou, W. W.-W., and Morris, P. J., "The Eigenvalue Spectrum of the Rayleigh Equation for a Plane Shear Layer," *International Journal for Numerical Methods in Fluids*, Vol. 15, No. 12, 1992, pp. 1407–1415. doi:10.1002/fld.1650151204.